



Cite this: *J. Mater. Chem. C*,  
2024, 12, 5916

# Enhanced stability and tunable optoelectronic properties of silicon–carbon monolayers by strain and surface functionalization†

Huabing Shu \* and Jiyuan Guo 

Exploring novel two-dimensional carbon-based materials with superior properties is of special importance for applications in nano-optoelectronics. Here, based on theoretical calculations, a silicon–carbon (Si<sub>2</sub>C) monolayer is explored, offering desirable properties with strain and surface functionalization. The pristine Si<sub>2</sub>C monolayer is dynamically unstable, but a small tensile strain of +2.5% and fluorination can make it more dynamically stable. The pristine Si<sub>2</sub>C monolayer is a direct semiconductor with a moderate bandgap, whose gap and exciton binding energy can be continuously tuned by strain engineering. Also, the tensile strain (fluorination) on the Si<sub>2</sub>C monolayer can induce a variation in optical transitions, thus resulting in a significant red-shift (blue-shift) of the optical absorption spectrum. In short, the Si<sub>2</sub>C monolayer under tensile strain and fluorination is unique, making it a promising candidate for nano-optoelectronics.

Received 28th January 2024,  
Accepted 27th March 2024

DOI: 10.1039/d4tc00401a

rsc.li/materials-c

## 1 Introduction

Group IV non-metal elements (C, Si) in the periodic table are fascinating. Hexagonal graphene composed of C atoms has attracted extensive interest owing to its high electron mobility ( $>2 \times 10^6 \text{ cm}^{-1} \text{ V}^{-1} \text{ s}^{-1}$ ),<sup>1</sup> extraordinary stiffness,<sup>2</sup> and high electron conductivity.<sup>3</sup> Unlike graphene, hexagonal silicene is a buckled structure with a buckling height of about 0.47 Å,<sup>4</sup> which is also expected to have outstanding properties.<sup>5–9</sup> However, both graphene and silicene have a Dirac cone at the Fermi level, suggesting their semimetal characteristics, which is a significant disadvantage for their use in optoelectronic devices. To achieve bandgap in graphene, carbon atoms of graphene were partially substituted with silicon atoms to form a new two-dimensional (2D) silicon carbide (named siligraphene), which has been regarded as a feasible method. Theoretical studies<sup>10–15</sup> have shown that siligraphenes with local minimal energies (such as SiC<sub>x</sub>,  $x = 1, 2, 3, 5, 6$ , and 7) exhibit graphene-like configurations. Compared to graphene, due to the ionic features of the Si–C bonds, most of these siligraphenes are verified to be direct or indirect semiconductors with moderate bandgaps. Previously, the bandgaps of siligraphenes have been predicted to be ~1.13 eV for SiC<sub>7</sub>,<sup>15</sup> ~0.78 eV for SiC<sub>6</sub>,<sup>14</sup> ~1.09 eV for SiC<sub>2</sub>,<sup>11</sup> and ~2.90 eV for SiC.<sup>10</sup> Among these siligraphenes, 2D SiC<sub>2</sub> has been synthesized by a reaction between exfoliated

graphene and a silicon source.<sup>16</sup> Until 2023, the honeycomb SiC monolayer had also been successfully produced by annealing thin films of transition metal carbides grown on 4H-SiC.<sup>17</sup>

Motivated by the recently synthesized 2D SiC and SiC<sub>2</sub>, we also predicted a siligraphene (Si<sub>2</sub>C monolayer) using first-principles calculations. However, the Si<sub>2</sub>C monolayer is dynamically unstable. Thus, we adopted strain and surface functionalization to investigate its behavior, which are experimentally achievable methods. In fact, atomically thin monolayers endow them with outstanding mechanical flexibility.<sup>18–20</sup> Previous experimental reports have shown that graphene has an intrinsic strength of 130 GPa, which can sustain a tensile strain of ~25%.<sup>21</sup> Theoretically, silicene can sustain a tensile strain of ~18% at the ultimate tensile strength point.<sup>22</sup> The MoS<sub>2</sub> monolayer is broken when the in-plane tensile strain is up to ~11% (broken strength of ~23 GPa).<sup>23</sup> Monolayer phosphorene can withstand a tensile strain of up to 30% along the armchair direction.<sup>24</sup> These indicate that 2D materials can offer a platform for strain engineering applications. Also, the strain on 2D materials can tune their properties.<sup>25,26</sup> In addition, for the mechanical strain in 2D materials, some developed methods, like atomic force microscopy-based nanoindentations,<sup>21</sup> high-resolution transmission electron microscopy fracture,<sup>27</sup> (piezoelectric) substrate-assisted tensile tests,<sup>28,29</sup> and micromechanical device-based tensile tests,<sup>30</sup> provide a platform for realizing tensile strains.

On the other hand, chemical functionalization<sup>31</sup> (like fluorination and hydrogenation) on 2D materials is also a mature technology, which has been realized in graphene<sup>32,33</sup> and germanene.<sup>34,35</sup> As a result, we applied biaxial tensile strain

School of Science, Jiangsu University of Science and Technology, Zhenjiang 212001, China. E-mail: shuhuabing@just.edu.cn

† Electronic supplementary information (ESI) available. See DOI: <https://doi.org/10.1039/d4tc00401a>

and fluorination on the Si<sub>2</sub>C monolayer to investigate its stability and electronic and optical properties by employing density-functional and many-body perturbation theories. These calculations showed that biaxial tensile strain and fluorination can greatly enhance its dynamical stability and tune its optoelectronic properties. The rest of this paper is organized as follows. In Section 2, the computational methods and details are described. In Section 3, the calculation results show the stability and electronic and optical properties of the Si<sub>2</sub>C monolayer under biaxial tensile strain and fluorination. Finally, the main findings are summarized in the conclusions.

## 2 Computational methods and details

The Quantum Espresso<sup>36</sup> and Yambo<sup>37</sup> codes based on density-functional and many-body perturbation theories were applied to optimize the structure and calculate the electronic and optical properties of the observed systems. The Perdew–Burke–Ernzerhof (PBE) functional<sup>38</sup> within the generalized gradient approximation, cutoff energy of 60 Ry for the plane-wave expansion, and a *k*-point mesh of 18 × 18 × 1 for sampling the Brillouin zone were considered to optimize the structures. The interaction between valence electrons and ions was described by norm-conserving pseudopotentials.<sup>39</sup> The convergences of 10<sup>−6</sup> Ry for the energy and 10<sup>−4</sup> Ry per a.u. for the atomic force were checked. A vacuum space of 24 Å was used to eliminate the coupling between adjacent cells along the lattice vector *c* direction. The phonon band structures of the systems were calculated using density functional perturbation theory<sup>40</sup> and the acoustic sum rule was used for the vibrational frequencies at the *G* point.

The *G*<sub>0</sub>*W*<sub>0</sub> method<sup>41,42</sup> was used to determine the quasi-particle band structures of the systems. An energy cutoff of 60 Ry for the response functions, a box-shaped truncated Coulomb potential after 28 a.u. along the *c* direction, a response cutoff of 12 Ry, and 1040 bands were used to obtain the convergence of the quasi-particle bandgap. Based on the *G*<sub>0</sub>*W*<sub>0</sub> results, the Tamm–Dancoff approximation<sup>43</sup> was considered in the Bethe–Salpeter Hamilton. Excitation energies and exciton wave functions were obtained by solving the Bethe–Salpeter equation (BSE):<sup>44,45</sup>

$$(E_{\text{ck}}^{\text{QP}} - E_{\text{vk}}^{\text{QP}})A_{\text{vck}}^{\text{S}} + \sum_{\mathbf{k}'\mathbf{v}'\mathbf{c}'} \langle \mathbf{v}\mathbf{c}\mathbf{k} | K^{\text{ch}} | \mathbf{v}'\mathbf{c}'\mathbf{k}' \rangle A_{\mathbf{v}'\mathbf{c}'\mathbf{k}'}^{\text{S}} = \Omega^{\text{S}} A_{\text{vck}}^{\text{S}} \quad (1)$$

where  $\Omega^{\text{S}}$ ,  $A_{\text{vck}}^{\text{S}}$ , and  $K^{\text{ch}}$  are the excitation energy, the amplitude of the electron–hole pair, and screened coupling between the electron and hole, respectively. Eight higher valence bands and sixteen lower conduction bands were used to calculate excitonic states. A *k*-mesh of 18 × 18 × 1 was interpolated to 36 × 36 × 1 to acquire converged optical spectra.

## 3 Results and discussion

### 3.1 Structural, electronic, and stable properties of the Si<sub>2</sub>C monolayer

Fig. 1a shows the optimized configuration of the Si<sub>2</sub>C monolayer with a hexagonal structure, in which a unit cell includes

two C atoms and four Si atoms. The relaxed Si<sub>2</sub>C monolayer has a lattice constant *a* (*b*) of 5.801 Å, which is much higher than that (5.027 Å) of a previously reported SiC<sub>2</sub> monolayer with a similar lattice structure.<sup>46</sup> The hexagonal honeycomb configuration is different from that of silicene with a buckling structure but is similar to that of planar graphene. The Si–Si and Si–C bond lengths (*l*<sub>Si–Si</sub>, *l*<sub>Si–C</sub>) were calculated to be 2.207 Å and 1.812 Å, respectively. They are similar to those in silicene (*l*<sub>Si–Si</sub> = 2.280 Å)<sup>4,47</sup> and the SiC<sub>2</sub> monolayer (*l*<sub>Si–C</sub> = 1.802 Å).<sup>46</sup> Fig. 1b shows the calculated quasi-particle band structure of the Si<sub>2</sub>C monolayer, in which the valence band maximum (VBM) and conduction band minimum (CBM) are both located at a high-symmetry *G* point, suggesting that it is a direct semiconductor. The estimated quasi-particle bandgap is 1.470 eV, which is very much desirable for applications in optoelectronic devices like photovoltaic and photocatalytic devices. The quasi-particle bandgap can correctly reflect the electronic energy gap of the semiconducting material due to the full consideration of electron–electron coupling. It is also worth noting that the quasi-particle bandgap calculated by the *G*<sub>0</sub>*W*<sub>0</sub> method is much larger than that obtained by the PBE method (0.678 eV). This is because the reduced electronic screening in the semiconducting monolayer can significantly enhance the Coulomb coupling between electrons. However, the PBE method does not completely consider Coulomb coupling, and thus seriously underestimates the electronic gap of the semiconducting monolayer. In fact, for the other semiconducting monolayers, this phenomenon has been reported previously, e.g., for Ga<sub>2</sub>STe (~1.91/0.94 eV for *G*<sub>0</sub>*W*<sub>0</sub>/PBE),<sup>48</sup> phosphorene (~2.00/0.83 eV for *G*<sub>0</sub>*W*<sub>0</sub>/PBE),<sup>49,50</sup> and MoS<sub>2</sub> (~2.82/1.60 eV for *G*<sub>0</sub>*W*<sub>0</sub>/PBE).<sup>51</sup> As a result, the quasi-particle bandgap based on the *G*<sub>0</sub>*W*<sub>0</sub> method is adopted as an electronic energy gap in this work.

In addition, the dynamical stability of the Si<sub>2</sub>C monolayer is examined by computing phonon dispersion, as presented in Fig. 1c. Three acoustic branches (ZA, TA, LA) and fifteen optical (O) branches of the Si<sub>2</sub>C monolayer are shown in Fig. 1c. The out-of-plane phonon mode (ZA) partially shifts to the negative frequency zone, with only a very small range near the *G* point. The maximum negative frequency is about −8.1 cm<sup>−1</sup> along the *G*–*M* direction. Usually, negative frequencies less than −10 cm<sup>−1</sup> can be neglected. However, a prominent optical phonon mode (marked by a red solid line) also falls in the negative frequency zone. The maximum imaginary frequency can be as large as about −91.6 cm<sup>−1</sup> at the *G* point, indicating that the pristine Si<sub>2</sub>C monolayer is dynamically very unstable. Although a negative optical branch is found, the phonon frequencies of the highest four optical branches can reach values in the range of 800–1000 cm<sup>−1</sup>, suggesting a strong atom bond in the Si<sub>2</sub>C monolayer. Further, the calculated density of phonon states indicates that the imaginary optical phonon mode originates from the contribution of the Si1 atom (marked in Fig. 1a), as shown in Fig. 1d. The imaginary optical phonon mode could be directly related to the bonding nature around the Si1 atom, where Si–Si sp<sup>2</sup>-like hybridization is observed. Usually, Si–Si bonds in silicon materials are formed by sp<sup>3</sup> hybridization (bulk silicon) or mixed sp<sup>2</sup>/sp<sup>3</sup>

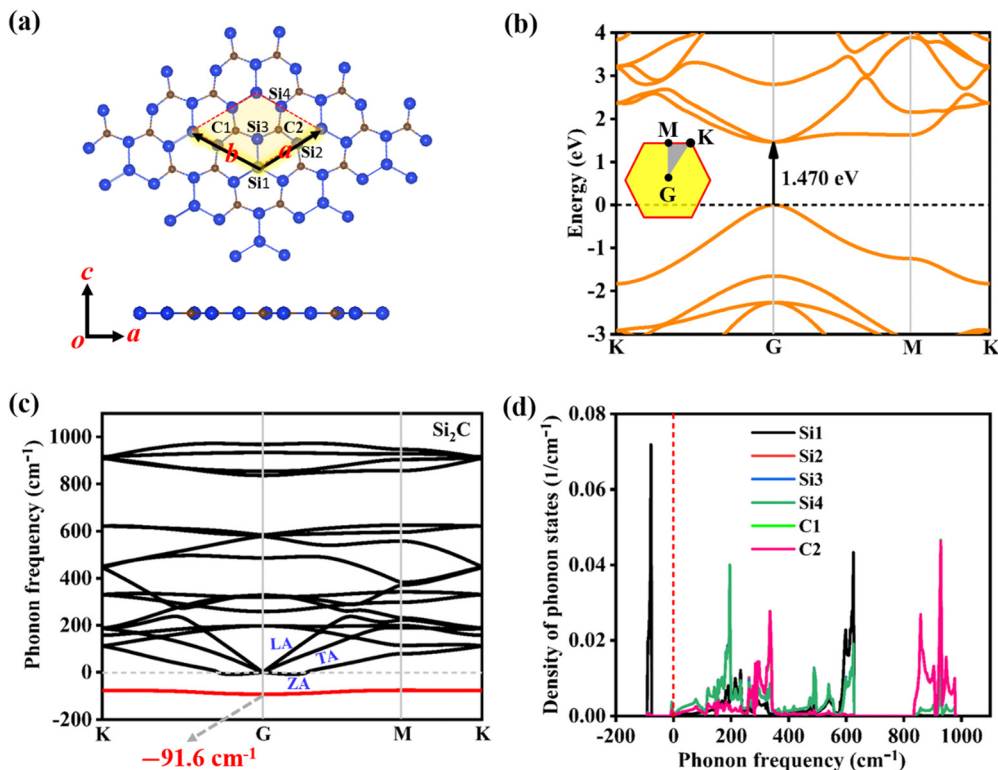


Fig. 1 (a) Top/side view, (b) quasi-particle band structure, (c) phonon spectrum, and (d) density of phonon states of the optimized  $\text{Si}_2\text{C}$  monolayer.

hybridization (silicene).<sup>47</sup> This suggests that the  $\text{Si}_2\text{C}$  monolayer with Si-Si  $\text{sp}^2$ -like hybridization is in a metastable state. The highest four optical modes are contributed by Si-C bonding. Although the  $\text{Si}_2\text{C}$  monolayer has a desirable gap, structural stability is a prerequisite for the development of  $\text{Si}_2\text{C}$  monolayer-based optoelectronic devices. Thus, the elimination of the imaginary optical phonon mode in the pristine  $\text{Si}_2\text{C}$  monolayer should be considered first. Here, biaxial strain and surface functionalization are used to investigate the  $\text{Si}_2\text{C}$  monolayer. The corresponding discussions are presented in Sections 3.2–3.4.

### 3.2 Strain effects on stability and electronic properties of the $\text{Si}_2\text{C}$ monolayer

Usually, biaxial compressive strain can easily induce an imaginary frequency in two-dimensional materials. Here, only the biaxial tensile strains are considered to investigate the dynamical stability of the  $\text{Si}_2\text{C}$  monolayer. Fig. 2 exhibits the phonon spectra of the  $\text{Si}_2\text{C}$  monolayer under biaxial tensile strains ( $\delta$ ) of +1 to +8%. The biaxial tensile strain  $\delta$  can be realized by stretching the lattice constant, *i.e.*  $\delta = (a_1 - a)/a$ , where  $a_1$  and  $a$  are the lattice constants of the strained and pristine systems, respectively. With an increased  $\delta$ , the maximum negative frequency in the  $\text{Si}_2\text{C}$  monolayer can be decreased from  $-70.2 \text{ cm}^{-1}$  ( $\delta = +1\%$ ) to  $-34.7 \text{ cm}^{-1}$  ( $\delta = +2\%$ ) and the negative optical branch is slowly lifted up. When the tensile strain is as high as +2.5%, the imaginary frequency is eliminated fully, as shown in Fig. 2c. During the fabrication of the  $\text{Si}_2\text{C}$  monolayer, a biaxial tensile strain of +2.5% can be

generated when it is deposited on different substrates. When the tensile strain is further increased from +2.5% to +8%, no imaginary frequency is found in the  $\text{Si}_2\text{C}$  monolayer and the highest four optical phonon modes are softened compared to the pristine structure, as seen in Fig. 2d–f. As a result, a relatively small biaxial tensile strain on the  $\text{Si}_2\text{C}$  monolayer can significantly improve its dynamical stability.

In fact, two-dimensional materials can withstand very large tensile strains before they are cracked.<sup>52</sup> For example, graphene and silicene can reach fracture tensile strains of approximately +30% and +19% at room temperature,<sup>53,54</sup> respectively. Thus, a wide tensile strain range of 0 to +19% is applied to the  $\text{Si}_2\text{C}$  monolayer. The strain energy ( $E_{\text{se}}$ ) in the  $\text{Si}_2\text{C}$  monolayer is investigated first, as shown in Fig. 3 (red solid pentagrams). The critical tensile strain was observed at  $\delta_1 = +18\%$ . Below the critical strain value,  $E_{\text{se}}$  constantly increases with an increased  $\delta$ , followed by a parabolic shape, indicating that a hexagonal honeycomb configuration can be retained in the tensile strain range of  $0 < \delta < +18\%$ . When the strain is higher than +18%,  $E_{\text{se}}$  suddenly decreases, indicating that the strained  $\text{Si}_2\text{C}$  monolayer enters the plastic region (irreversible deformation) from the elastic region. In addition, the derivative curve of  $E_{\text{se}}$  with respect to  $\delta$  is also depicted in Fig. 3 (blue solid circles). The first-order derivative  $dE_{\text{se}}(\delta)/d\delta$  reaches a maximum value at  $\delta_2 = +15\%$  (indicated by the black arrow in Fig. 3); then it slowly decreases when  $\delta$  is further increased, indicating that the structure can be further expanded by a small tensile strain and becomes unstable. Fig. S1 of the ESI† shows the calculated phonon spectra of the  $\text{Si}_2\text{C}$  monolayer at tensile strains of

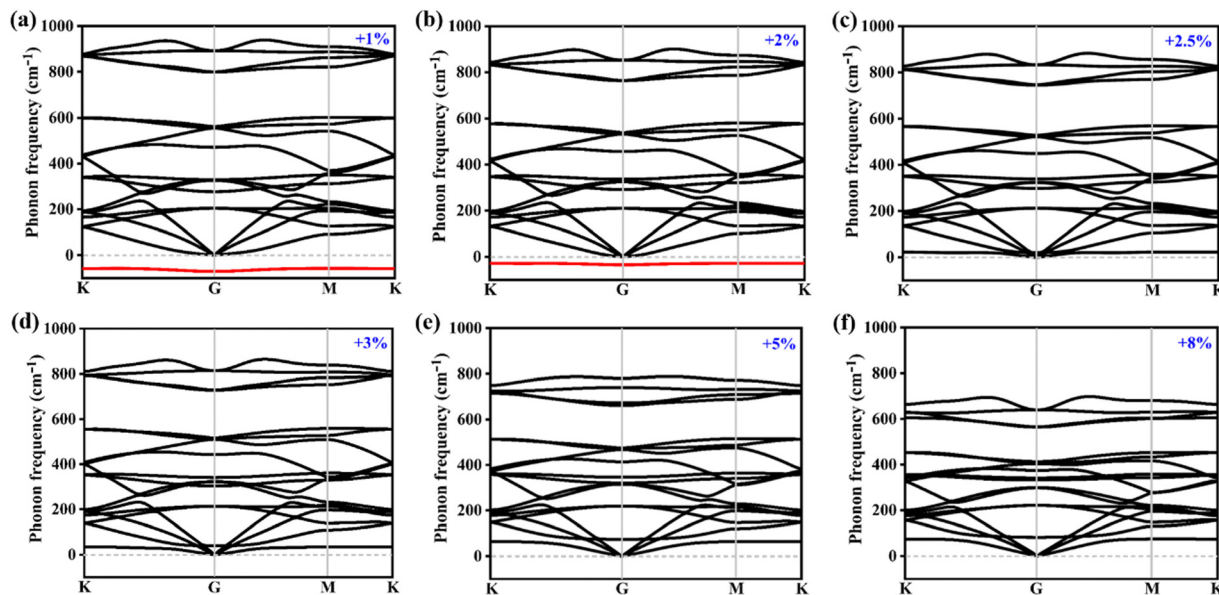


Fig. 2 Phonon spectra of the Si<sub>2</sub>C monolayer under different tensile strains: (a) +1%, (b) +2%, (c) +2.5%, (d) +3%, (e) +5%, and (f) +8%.

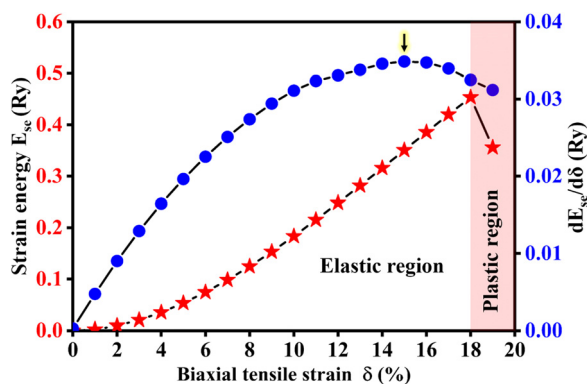


Fig. 3 Variable strain energy  $E_{se}$  of the Si<sub>2</sub>C monolayer and its derivation with respect to tensile strain  $\delta$ .  $E_{se}$  is defined as the total energy difference between the strained and pristine systems, namely,  $E_{se} = E_{total}(\delta) - E_{total}(0)$ .

$\delta = +15\%$  and  $+16\%$ . The outstanding imaginary phonon frequencies at a tensile strain of  $+16\%$  were observed, suggesting that the system remains in the metastable configuration in the tensile strain range of  $+15\% < \delta < +18\%$ .

The second-order derivative of  $E_{se}$  is also calculated, which can throw light on the strength of the two-dimensional system. It is closely related to the in-plane stiffness ( $C$ ). In the elastic strain range,  $C$  is defined *via* the expression<sup>55,56</sup>  $C = \frac{1}{S_0} \frac{d^2 E_{se}}{d\delta^2}$ , where  $S_0$  is the equilibrium surface area of the pristine Si<sub>2</sub>C monolayer. The in-plane stiffness of the Si<sub>2</sub>C monolayer is predicted to be about  $135 \text{ N m}^{-1}$ , which is lower than those of the other honeycomb monolayers like SiC<sub>2</sub> ( $393 \text{ N m}^{-1}$ ),<sup>46</sup> graphene ( $340 \text{ N m}^{-1}$ ),<sup>21</sup> and SiC ( $166 \text{ N m}^{-1}$ ).<sup>55</sup> However, it is much higher than that of silicene ( $62 \text{ N m}^{-1}$ ) with a broad strain adjustment.<sup>55</sup> The size of the in-plane stiffness in the Si<sub>2</sub>C monolayer indicates that it can be manipulated by strain

engineering in the experiment, thus tuning the physical properties of the Si<sub>2</sub>C monolayer for use in different optoelectronic devices.

Fig. 4a displays the mutable quasi-particle energy bandgaps of the Si<sub>2</sub>C monolayer under different biaxial tensile strains of  $\delta = 0$  to  $+8\%$ . With enhanced tensile strain, the quasi-particle bandgap decreased almost linearly from  $1.470 \text{ eV}$  ( $\delta = 0$ ) to  $0.986 \text{ eV}$  ( $\delta = +8\%$ ) at the  $G_0W_0$  level. The linear dependence of the quasi-particle bandgap on the strain originates from the deformation potential, *i.e.* the strain-induced band downshifting.<sup>57,58</sup> In fact, this phenomenon has also been reported previously for semiconducting silicon and germanium.<sup>59,60</sup> The direct nature of the bandgap of the strained Si<sub>2</sub>C monolayer is retained in the observed strain range, as seen in Fig. 4b–d. Due to the increase of the tensile strain, the distance between the neighboring atoms becomes large, which directly leads to the reduction of the orbital overlap between the neighboring atoms, inducing a change of the orbital energy. The partial charge densities of the VBM and CBM of the Si<sub>2</sub>C monolayer are also exhibited under different strains ( $\delta = 0, +3\%$ , and  $+8\%$ ), as shown in Fig. S2 of the ESI.† It can be clearly seen that the CBM has been significantly influenced, while the VBM is almost unchanged. The remarkable charge change of the CBM can move the CBM down, thus reducing the bandgap of the Si<sub>2</sub>C monolayer with increasing tensile strain. It is also worth noting that the third conduction band at the  $G$  point is very sensitive to tensile strain, as indicated by the black dotted circle in Fig. 4b and c. When the strain is higher than  $+8\%$ , the third conduction band becomes the CBM and the bandgap further decreases to zero at  $\delta = +12\%$  (as shown in Fig. S3 of the ESI.†). The following discussion will focus on the optical properties of the Si<sub>2</sub>C monolayer under moderate tensile strains of  $0$  to  $+8\%$  due to the suitable bandgap applied in optoelectronics.



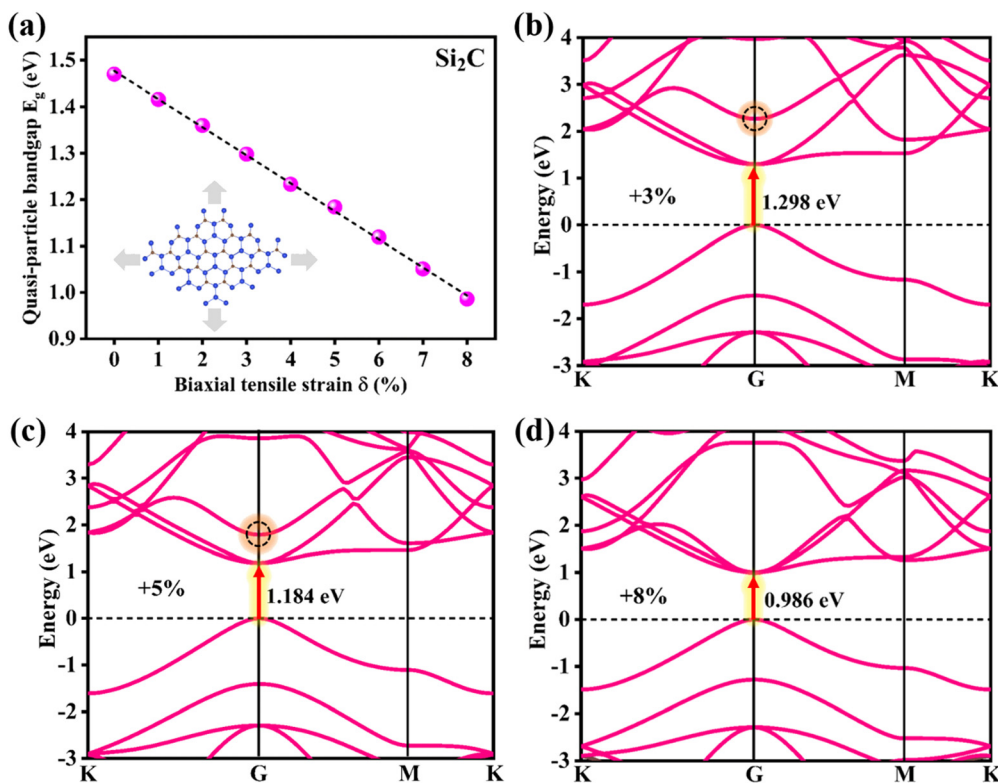


Fig. 4 (a) Quasi-particle energy bandgap as a function of tensile strain  $\delta$  for the  $\text{Si}_2\text{C}$  monolayer. (b)–(d) Quasi-particle band structures of the  $\text{Si}_2\text{C}$  monolayer at tensile strains of +3%, +5%, and +8%.

### 3.3 Strain effects on the optical properties of the $\text{Si}_2\text{C}$ monolayer

Compared with the bulk, atomically thin two-dimensional monolayers have significantly enhanced electron–electron ( $e$ – $e$ ) and electron–hole ( $e$ – $h$ ) couplings. At present, the  $G_0W_0$  + BSE method has been regarded as an optimal method to obtain the exact optical properties of the monolayers, where the  $G_0W_0$  and BSE methods can perform well with the  $e$ – $e$  and  $e$ – $h$  couplings, respectively. Based on the quasi-particle band structures, the incident light frequency-dependent dielectric constant  $\varepsilon(\omega)$  of the  $\text{Si}_2\text{C}$  monolayer can be obtained by solving the Bethe–Salpeter equation.  $\varepsilon(\omega)$  is made up of the real part  $\varepsilon_1(\omega)$  and imaginary part  $\varepsilon_2(\omega)$ , *i.e.*,  $\varepsilon(\omega) = \varepsilon_1(\omega) + i\varepsilon_2(\omega)$ .  $\varepsilon_2(\omega)$  is referred to as the dissipation channel for the transition, which results in the optical absorption peaks, thus determining the optical absorption of the system. In addition, the depolarization effects in the 2D material are very significant for the incident polarized light vertical to the surface of the 2D material (*i.e.* the lattice vector  $c$  direction); that is the optical absorption for the in-plane polarized light is far greater than that of the out-of-plane polarized light. This was also verified in the  $\text{Si}_2\text{C}$  monolayer, as shown in Fig. S4 of the ESI†; thus, only the optical properties were investigated for polarized light parallel to the surface (along the lattice vector  $a$ , as shown in Fig. 1a).

Fig. 5a shows the  $\varepsilon_2(\omega)$  of the pristine  $\text{Si}_2\text{C}$  monolayer using the  $G_0W_0$  + BSE and  $G_0W_0$  + RPA methods along the lattice vector  $a$ . Compared with that of the  $G_0W_0$  + RPA (excluding the

$e$ – $h$  coupling), the optical spectrum from the  $G_0W_0$  + BSE shows a significant red-shift, suggesting the importance of  $e$ – $h$  coupling in the  $\text{Si}_2\text{C}$  monolayer. It also exhibits a broad absorption range from near-infrared to near-ultraviolet light (0.5–4 eV). For a direct semiconductor, the first absorption peak is particularly meaningful. The position of the peak, *i.e.* the excitation energy  $E_{ee}$ , is known as the optical gap of the system and can be measured experimentally. For the  $\text{Si}_2\text{C}$  monolayer, the first absorption peak with a maximum oscillator of 1 is located at an energy of  $E_{ee} = 0.849$  eV (below the  $G_0W_0$  bandgap  $E_{g-G_0W_0} = 1.470$  eV), corresponding to a bright bound exciton state. In light of the oscillator strength selection rule, the first absorption peak is confirmed to originate from the VBM  $\rightarrow$  CBM vertical transition at the  $G$  point. Thus, the binding energy ( $E_{eb}$ ) of the bright bound exciton is predicted to be 0.621 eV by the energy difference between  $E_{g-G_0W_0}$  and the excitation energy  $E_{ee}$ , *i.e.*  $E_{eb} = E_{g-G_0W_0} - E_{ee}$ . Such a significant binding energy of excitons is useful for effectively confining both photogenerated electrons and holes, greatly slowing down their recombination, thus increasing the light utilization efficiency. This is a very huge advantage compared to that of the semiconducting bulk (less than 50 meV)<sup>49,61,62</sup>.

Next, the strain-dependent optical properties of the  $\text{Si}_2\text{C}$  monolayer are also evaluated for potential application in optoelectronics. Fig. 5b shows the  $\varepsilon_2$  of the  $\text{Si}_2\text{C}$  monolayer in the biaxial tensile strain range of  $0 < \delta < +8\%$ , in which the first absorption peak is found at 0.849 eV, 0.713 eV, 0.628 eV,

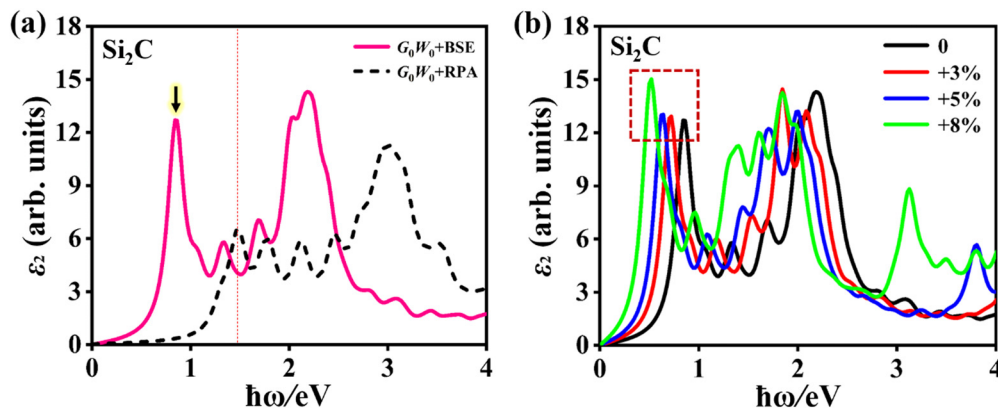


Fig. 5 (a) Imaginary part ( $\epsilon_2$ ) of the dielectric function of the Si<sub>2</sub>C monolayer from  $G_0W_0$  + BSE and  $G_0W_0$  + RPA calculations for the polarized light along the lattice vector  $a$  direction. The red dotted dashed line shows the position of the quasi-particle bandgap (1.47 eV). (b)  $\epsilon_2$  of the Si<sub>2</sub>C monolayer as a function of photon energy ( $\hbar\omega$ ) at different tensile strains of  $\delta = 0, +3\%, +5\%$ , and  $+8\%$ , employing the  $G_0W_0$  + BSE method. A Lorentzian broadening of 0.10 eV is adopted in these curves.

**Table 1** Excitation energy ( $E_{ee}$ ), exciton binding energy ( $E_{eb}$ ), and exciton radius ( $R_{er}$ ), corresponding to the first absorption peak in the strained Si<sub>2</sub>C monolayer.  $E_{g-G_0W_0}$  is the quasi-particle energy bandgap at the  $G_0W_0$  level. Units of energy and radius are eV and Å, respectively

Strain	$E_{ee}$	$E_{g-G_0W_0}$	$E_{eb}$	$R_{er}$
0	0.849	1.470	0.621	31.36
+3%	0.713	1.298	0.585	33.47
+5%	0.626	1.184	0.556	36.25
+8%	0.511	0.986	0.475	43.51

0.511 eV for tensile strains  $\delta = 0, +3\%, +5\%$ , and  $+8\%$ , respectively. The first absorption peak is dramatically red-shifted by approximately 0.338 eV under a tensile strain of  $+8\%$ . Such a red-shift of the absorption curve causes a significant enhancement for near-infrared light, which should be attributed to the decreased bandgap. The first absorption peaks in the strained systems are formed by the VBM–CBM vertical transition at the  $G$  point. The binding energies of the bright bound excitons corresponding to the first absorption peaks are also calculated to be 0.585 eV ( $\delta = +3\%$ ), 0.556 eV ( $\delta = +5\%$ ), and 0.475 eV ( $\delta = +8\%$ ), as listed in Table 1. The estimated  $E_{eb}$  is reduced by 146 meV from 0.621 eV ( $\delta = 0$ ) to 0.475 eV ( $\delta = +8\%$ ), indicating that  $E_{eb}$  can be tuned by the tensile strains and first bright bound exciton still has high stability at a large tensile strain of  $+8\%$ .

Further, these bright bound excitons in the strained Si<sub>2</sub>C monolayer are also investigated. The normalized squared exciton wave function  $|\psi(r_e, r_h)|^2$  is obtained by  $|\psi(r_e, r_h)\rangle = \sum_{c\mathbf{k}} A_{vc\mathbf{k}}^S \psi_{c\mathbf{k}}(r_e) \psi_{v\mathbf{k}}(r_h)$ , where  $r_e$  and  $r_h$  are the real-space electron and hole coordinates, respectively. The calculated hole (red solid sphere) is located at the center of a supercell with dimensions  $30 \times 30 \times 1$ . Fig. 6 presents the real-space distribution of the electron. It can be clearly seen that the bright bound exciton in the pristine Si<sub>2</sub>C monolayer is more spatially localized than those in the strained Si<sub>2</sub>C monolayer. The estimated exciton radii ( $R_{er}$ ) are about 31.36 Å, 33.47 Å, 36.25 Å, and 43.51 Å for  $\delta = 0, +3\%, +5\%$ , and  $+8\%$ , respectively.

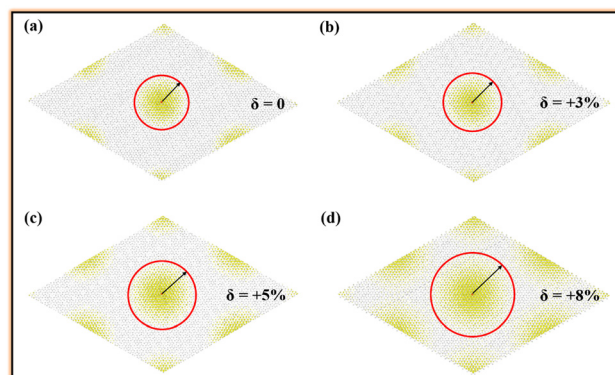


Fig. 6 Top view of real-space electron probability distribution corresponding to the first bright bound excitons in the strained Si<sub>2</sub>C monolayer: (a)  $\delta = 0$ , (b)  $\delta = +3\%$ , (c)  $\delta = +5\%$ , and (d)  $\delta = +8\%$ . The red solid sphere represents the hole position. To clearly see the electron distribution, all atoms are marked by gray spheres.

This indicates that a larger binding energy of an exciton can induce a smaller extended electron distribution in real space; thus, a weaker electronic screening is found in a smaller, strained system. This also suggests that the electron–hole pairs in the relatively large strain are easier to separate. As a result, the separated electrons and holes in the strained Si<sub>2</sub>C monolayer could be applied to improve the performance of optoelectronic devices based on the Si<sub>2</sub>C monolayer.

To further exhibit the light-harvesting ability of the Si<sub>2</sub>C monolayer for the sunlight under the biaxial tensile strain, the light absorption coefficient is also calculated by the following equation:<sup>63</sup>

$$\alpha(\omega) = \frac{\sqrt{2}\omega}{c} \left[ \sqrt{\epsilon_1^2(\omega) + \epsilon_2^2(\omega)} - \epsilon_1(\omega) \right]^{\frac{1}{2}} \quad (2)$$

where  $c$  is the velocity of light in a vacuum. As shown in Fig. 7, the light absorption intensity can be higher than  $10^5 \text{ cm}^{-1}$  for the energy range of 0.5–4 eV, indicating a strong light

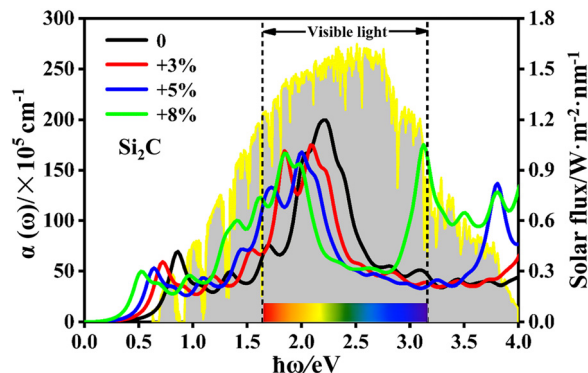


Fig. 7 Light absorption coefficient  $\alpha(\omega)$  of the  $\text{Si}_2\text{C}$  monolayer under different tensile strains (0, +3%, +5%, +8%) as a function of photon energy ( $\hbar\omega$ ). The incident solar irradiance at air mass 1.5G is considered for comparison.

absorption ability from the near-infrared to near-ultraviolet region for the observed strained systems. For the pristine (+8% strained)  $\text{Si}_2\text{C}$  monolayer, the maximum absorption intensity was  $2.01 \times 10^7$  ( $1.66 \times 10^7$ )  $\text{cm}^{-1}$  at a photon energy of 2.21 (1.83) eV. Compared to infrared light, visible light,

which accounts for about 43% of sunlight, is much more active in the observed strained systems. The absorption coefficients in the visible light region are also comparable to those of other light-harvesting monolayers, like  $\text{Pd}_2\text{Se}_3$ :<sup>64</sup>  $\sim 10^6$   $\text{cm}^{-1}$ , fluorinated  $\text{CP}_3$ :<sup>65</sup>  $\sim 10^5$   $\text{cm}^{-1}$ ,  $\text{MoSi}_2\text{N}_4$ :<sup>66</sup>  $\sim 10^5$   $\text{cm}^{-1}$ . As a result, strained  $\text{Si}_2\text{C}$  monolayers can be considered as candidates for optoelectronic devices owing to their effective utilization of sunlight.

### 3.4 Fluorination effects on stable, electronic and optical properties

The optimized configuration of the fully fluorinated  $\text{Si}_2\text{C}$  monolayer ( $\text{Si}_4\text{C}_2\text{F}_6$ ) is shown in Fig. 8a, where the lattice constant  $a/b$  is 5.829 Å and  $l_{\text{Si-Si}}$  ( $l_{\text{Si-C}}$ ) is 2.356 (1.928) Å. These lattice parameters are higher than those of pristine  $\text{Si}_2\text{C}$  monolayer. Due to full fluorination, the planar configuration was transformed to the buckled configuration. The buckled  $\text{Si}_4\text{C}_2\text{F}_6$  is similar to previously reported fluorinated silicene and fluorinated graphene.<sup>47</sup> The Si-F and C-F bond lengths are predicted to be about 1.611 Å and 1.456 Å, respectively, which are very close to those in fluorinated silicene and fluorinated graphene (1.620 Å; 1.390 Å).<sup>47</sup> Although  $\text{Si}_4\text{C}_2\text{F}_6$  is a buckling structure,

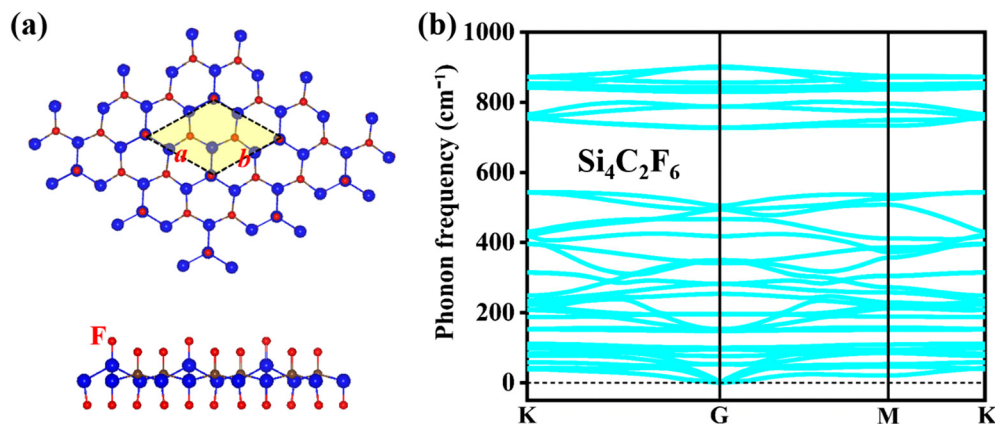


Fig. 8 (a) Top and side views and (b) phonon spectrum of the fluorinated  $\text{Si}_2\text{C}$  monolayer ( $\text{Si}_4\text{C}_2\text{F}_6$ ).

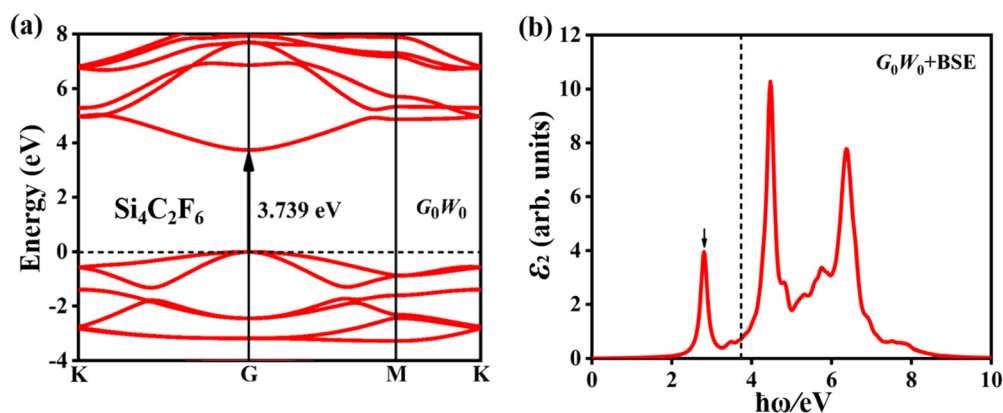


Fig. 9 (a) Quasi-particle band structure and (b) imaginary part ( $\epsilon_2$ ) of the dielectric function of  $\text{Si}_4\text{C}_2\text{F}_6$ . The dashed line indicates the position corresponding to the quasi-particle bandgap.

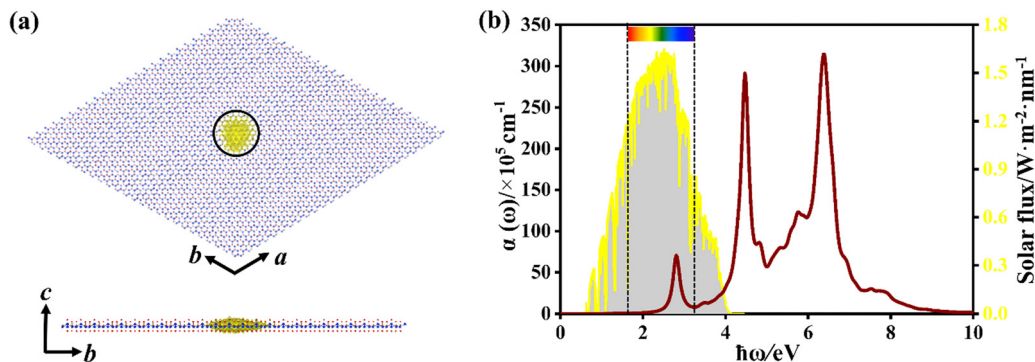


Fig. 10 (a) Top and side views of real-space electron probability distribution corresponding to the first bright excitons in  $\text{Si}_4\text{C}_2\text{F}_6$ . Yellow indicates electron distribution. The supercell used is  $24 \times 24 \times 1$ . (b) Light absorption coefficient  $\alpha(\omega)$  of  $\text{Si}_4\text{C}_2\text{F}_6$  as a function of the photon energy ( $\hbar\omega$ ). The incident solar irradiance at air mass 1.5G is provided for comparison. The two dashed lines indicate the visible-light region.

the hexagonal lattice is still retained. Compared to the pristine  $\text{Si}_2\text{C}$  monolayer, the different lattice parameters of  $\text{Si}_4\text{C}_2\text{F}_6$  can cause different phonon dispersions and band structures. Fig. 8b exhibits the calculated phonon spectrum of  $\text{Si}_4\text{C}_2\text{F}_6$ , in which the negative frequencies induced by the Si1 atom in the pristine  $\text{Si}_2\text{C}$  monolayer were eliminated by fluorination. This indicates that  $\text{Si}_4\text{C}_2\text{F}_6$  is dynamically stable, suggesting that fluorination is an effective way to enhance the dynamical stability of the  $\text{Si}_2\text{C}$  monolayers.

Fig. 9a shows the quasi-particle band structure of  $\text{Si}_4\text{C}_2\text{F}_6$ , in which it is still a direct-gap semiconductor at the  $G$  point. The estimated gap is 3.739 eV, which is much larger than that of the pristine  $\text{Si}_2\text{C}$  monolayer (1.470 eV). It is between 7.010 eV for fluorinated graphene and 2.760 eV for fluorinated silicene.<sup>47</sup> Such a large gap can induce large absorption of incident near-ultraviolet light, as shown in Fig. 9b. Compared with that of the pristine  $\text{Si}_2\text{C}$  monolayer, the optical spectrum of  $\text{Si}_4\text{C}_2\text{F}_6$  was blue-shifted significantly due to the large electronic bandgap. The first absorption peak is located at 2.806 eV, and originates from the VBM  $\rightarrow$  CBM vertical transition; thus, a bright bound exciton is formed. The exciton binding energy was estimated to be 0.933 eV, which is significantly higher than that of the pristine  $\text{Si}_2\text{C}$  monolayer (0.621 eV). This can induce a relative localization of electrons, thus resulting in a small exciton radius of 11.03 Å, as shown in Fig. 10a. In addition, the absorption coefficient can attain a value of  $10^7 \text{ cm}^{-1}$  for near-ultraviolet light, as seen in Fig. 10b. These results indicate that  $\text{Si}_4\text{C}_2\text{F}_6$  can be used in optoelectronic devices based on wide-gap semiconductors like ultraviolet photodetectors and sensors.

## 4 Conclusions

In conclusion, the structural stability, quasi-particle band structures, and optical properties of  $\text{Si}_2\text{C}$  monolayers were systematically investigated under tensile strain and fluorination. The pristine  $\text{Si}_2\text{C}$  monolayer had a moderate in-plane stiffness of  $135 \text{ N m}^{-1}$ , ensuring that it could be manipulated experimentally by strain engineering. A biaxial tensile strain between +2.5% and +15% can maintain the dynamical stability

of the structure. The quasi-particle bandgap of the  $\text{Si}_2\text{C}$  monolayer at the  $G_0W_0$  level could be linearly tuned from 1.470 eV ( $\delta = 0$ ) to 0.986 eV ( $\delta = +8\%$ ), even becoming a semimetal at a tensile strain of +12%. The increased tensile strain leads to a significant red-shift of the optical absorption spectrum, thus enhancing the absorption for the near-infrared light. The pristine  $\text{Si}_2\text{C}$  monolayer had a large exciton binding energy of 0.621 eV, suggesting that the photogenerated electrons and holes could not be easily recombined by external perturbations. More importantly, when the tensile strain is increased to +8%, the binding energy of the bright bound exciton corresponding to the first absorption peak only decreased by 146 meV, indicating that the observed exciton is still stable in the relatively large tensile strain range. In addition, fluorination can cause a large quasi-particle bandgap of 3.739 eV with direct characteristics and a considerable exciton binding energy of 0.933 eV in the  $\text{Si}_2\text{C}$  monolayer. These results are very important for the application of  $\text{Si}_2\text{C}$  monolayers in nanoelectronic and optoelectronic devices.

## Conflicts of interest

There are no conflicts to declare.

## Acknowledgements

The authors gratefully acknowledge financial support from the Jiangsu University of Science and Technology (No. 1052931610).

## References

- 1 K. I. Bolotin, K. J. Sikes, Z. Jiang, M. Klima, G. Fudenberg, J. Hone, P. Kim and H. L. Stormer, *Solid State Commun.*, 2008, **146**, 351–355.
- 2 T. J. Booth, P. Blake, R. R. Nair, D. Jiang, E. W. Hill, U. Bangert, A. Bleloch, M. Gass, K. S. Novoselov, M. I. Katsnelson and A. K. Geim, *Nano Lett.*, 2008, **8**, 2442–2446.
- 3 M. Liu, X. Yin, E. Ulin-Avila, B. Geng, T. Zentgraf, L. Ju, F. Wang and X. Zhang, *Nature*, 2011, **474**, 64–67.



- 4 H. Shu, *J. Mater. Sci.*, 2021, **56**, 5684–5696.
- 5 L. C. Lew Yan Voon, J. Zhu and U. Schwingenschlögl, *Appl. Phys. Rev.*, 2016, **3**, 040802.
- 6 B. D. Hoi, M. Yarmohammadi and H. A. Kazzaz, *J. Magn. Magn. Mater.*, 2017, **439**, 203–212.
- 7 M. Yarmohammadi, *RSC Adv.*, 2017, **7**, 10650–10659.
- 8 D. Z. Jakovljević, M. M. Grujić, M. Ž. Tadić and F. M. Peeters, *J. Phys.: Condens. Matter*, 2017, **30**, 035301.
- 9 M. Yarmohammadi, *J. Magn. Magn. Mater.*, 2017, **426**, 621–628.
- 10 H. C. Hsueh, G. Y. Guo and S. G. Louie, *Phys. Rev. B: Condens. Matter Mater. Phys.*, 2011, **84**, 085404.
- 11 L.-J. Zhou, Y.-F. Zhang and L.-M. Wu, *Nano Lett.*, 2013, **13**, 5431–5436.
- 12 M. Zhao and R. Zhang, *Phys. Rev. B: Condens. Matter Mater. Phys.*, 2014, **89**, 195427.
- 13 H. Dong, L. Wang, L. Zhou, T. Hou and Y. Li, *Carbon*, 2017, **113**, 114–121.
- 14 X. Liu, X. Shao, B. Yang and M. Zhao, *Nanoscale*, 2018, **10**, 2108–2114.
- 15 H. Dong, L. Zhou, T. Frauenheim, T. Hou, S.-T. Lee and Y. Li, *Nanoscale*, 2016, **8**, 6994–6999.
- 16 S. Lin, S. Zhang, X. Li, W. Xu, X. Pi, X. Liu, F. Wang, H. Wu and H. Chen, *J. Phys. Chem. C*, 2015, **119**, 19772–19779.
- 17 C. M. Polley, H. Fedderwitz, T. Balasubramanian, A. A. Zakharov, R. Yakimova, O. Bäcke, J. Ekman, S. P. Dash, S. Kubatkin and S. Lara-Avila, *Phys. Rev. Lett.*, 2023, **130**, 076203.
- 18 G. G. Naumis, S. Barraza-Lopez, M. Oliva-Leyva and H. Terrones, *Rep. Prog. Phys.*, 2017, **80**, 096501.
- 19 C. Si, Z. Sun and F. Liu, *Nanoscale*, 2016, **8**, 3207–3217.
- 20 J. Du, H. Yu, B. Liu, M. Hong, Q. Liao, Z. Zhang and Y. Zhang, *Small Methods*, 2021, **5**, 2000919.
- 21 C. Lee, X. Wei, J. W. Kysar and J. Hone, *Science*, 2008, **321**, 385–388.
- 22 B. Mortazavi, O. Rahaman, M. Makaremi, A. Dianat, G. Cuniberti and T. Rabczuk, *Phys. E*, 2017, **87**, 228–232.
- 23 S. Bertolazzi, J. Brivio and A. Kis, *ACS Nano*, 2011, **5**, 9703–9709.
- 24 Q. Wei and X. Peng, *Appl. Phys. Lett.*, 2014, **104**, 251915.
- 25 S. Wang, M. S. Ukhtary and R. Saito, *Phys. Rev. Res.*, 2020, **2**, 033340.
- 26 S. Wang, H. Tian and M. Sun, *J. Phys.: Condens. Matter*, 2023, **35**, 304002.
- 27 A. Azizi, X. Zou, P. Ercius, Z. Zhang, A. L. Elías, N. Perea-López, G. Stone, M. Terrones, B. I. Yakobson and N. Alem, *Nat. Commun.*, 2014, **5**, 4867.
- 28 G. Tsoukleri, J. Parthenios, K. Papagelis, R. Jalil, A. C. Ferrari, A. K. Geim, K. S. Novoselov and C. Galiotis, *Small*, 2009, **5**, 2397–2402.
- 29 F. Ding, H. Ji, Y. Chen, A. Herklotz, K. Dörr, Y. Mei, A. Rastelli and O. G. Schmidt, *Nano Lett.*, 2010, **10**, 3453–3458.
- 30 K. Cao, S. Feng, Y. Han, L. Gao, T. Hue Ly, Z. Xu and Y. Lu, *Nat. Commun.*, 2020, **11**, 284.
- 31 X. Tang, T. Fan, C. Wang and H. Zhang, *Small*, 2021, **17**, 2005640.
- 32 W. Feng, P. Long, Y. Feng and Y. Li, *Adv. Sci.*, 2016, **3**, 1500413.
- 33 X. Chen, K. Fan, Y. Liu, Y. Li, X. Liu, W. Feng and X. Wang, *Adv. Mater.*, 2022, **34**, 2101665.
- 34 N. Liu, G. Bo, Y. Liu, X. Xu, Y. Du and S. X. Dou, *Small*, 2019, **15**, 1805147.
- 35 T. Hartman, J. Šturala, J. Luxa and Z. Sofer, *ACS Nano*, 2020, **14**, 7319–7327.
- 36 P. Giannozzi, S. Baroni, N. Bonini, M. Calandra, R. Car, C. Cavazzoni, D. Ceresoli, G. L. Chiarotti, M. Cococcioni, I. Dabo, A. Dal Corso, S. de Gironcoli, S. Fabris, G. Fratesi, R. Gebauer, U. Gerstmann, C. Gougoussis, A. Kokalj, M. Lazzeri, L. Martin-Samos, N. Marzari, F. Mauri, R. Mazzarello, S. Paolini, A. Pasquarello, L. Paulatto, C. Sbraccia, S. Scandolo, G. Sclauzero, A. P. Seitsonen, A. Smogunov, P. Umari and R. M. Wentzcovitch, *J. Phys.: Condens. Matter*, 2009, **21**, 395502.
- 37 A. Marini, C. Hogan, M. Grüning and D. Varsano, *Comput. Phys. Commun.*, 2009, **180**, 1392–1403.
- 38 J. P. Perdew, K. Burke and M. Ernzerhof, *Phys. Rev. Lett.*, 1996, **77**, 3865–3868.
- 39 N. Troullier and J. L. Martins, *Phys. Rev. B: Condens. Matter Mater. Phys.*, 1991, **43**, 1993.
- 40 S. Baroni, S. de Gironcoli, A. Dal Corso and P. Giannozzi, *Rev. Mod. Phys.*, 2001, **73**, 515–562.
- 41 L. Hedin, *Phys. Rev.*, 1965, **139**, A796–A823.
- 42 M. S. Hybertsen and S. G. Louie, *Phys. Rev. B: Condens. Matter Mater. Phys.*, 1986, **34**, 5390.
- 43 A. L. Fetter and J. D. Walecka, *Quantum Theory of Many-Particle Systems*, Dover, New York, 2003, ch. 15, p. 565.
- 44 E. E. Salpeter and H. A. Bethe, *Phys. Rev.*, 1951, **84**, 1232.
- 45 G. Onida, L. Reining and A. Rubio, *Rev. Mod. Phys.*, 2002, **74**, 601–659.
- 46 H. Shu, *Appl. Surf. Sci.*, 2021, **559**, 149956.
- 47 W. Wei and T. Jacob, *Phys. Rev. B: Condens. Matter Mater. Phys.*, 2013, **88**, 045203.
- 48 H. Shu, *Phys. Chem. Chem. Phys.*, 2023, **25**, 7937–7945.
- 49 V. Tran, R. Soklaski, Y. Liang and L. Yang, *Phys. Rev. B: Condens. Matter Mater. Phys.*, 2014, **89**, 235319.
- 50 H. Shu, Y. Li, X. Niu and J. Wang, *Phys. Chem. Chem. Phys.*, 2016, **18**, 6085–6091.
- 51 A. Ramasubramaniam, *Phys. Rev. B: Condens. Matter Mater. Phys.*, 2012, **86**, 115409.
- 52 J. Annett and G. L. W. Cross, *Nature*, 2016, **535**, 271–275.
- 53 Q. X. Pei, Y. W. Zhang and V. B. Shenoy, *Carbon*, 2010, **48**, 898–904.
- 54 Q.-X. Pei, Z.-D. Sha, Y.-Y. Zhang and Y.-W. Zhang, *J. Appl. Phys.*, 2014, **115**, 023519.
- 55 H. Şahin, S. Cahangirov, M. Topsakal, E. Bekaroglu, E. Akturk, R. T. Senger and S. Ciraci, *Phys. Rev. B: Condens. Matter Mater. Phys.*, 2009, **80**, 155453.
- 56 M. Topsakal, S. Cahangirov and S. Ciraci, *Appl. Phys. Lett.*, 2010, **96**, 091912.
- 57 C. G. Van de Walle, *Phys. Rev. B: Condens. Matter Mater. Phys.*, 1989, **39**, 1871–1883.
- 58 Z. Liu, J. Wu, W. Duan, M. G. Lagally and F. Liu, *Phys. Rev. Lett.*, 2010, **105**, 016802.

- 59 M. V. Fischetti and S. E. Laux, *J. Appl. Phys.*, 1996, **80**, 2234–2252.
- 60 D. Yu, Y. Zhang and F. Liu, *Phys. Rev. B: Condens. Matter Mater. Phys.*, 2008, **78**, 245204.
- 61 W. Shan, B. D. Little, A. J. Fischer, J. J. Song, B. Goldenberg, W. G. Perry, M. D. Bremser and R. F. Davis, *Phys. Rev. B: Condens. Matter Mater. Phys.*, 1996, **54**, 16369–16372.
- 62 T. Cheiwchanchamnangij and W. R. L. Lambrecht, *Phys. Rev. B: Condens. Matter Mater. Phys.*, 2012, **85**, 205302.
- 63 X. Liu, P. Gao, W. Hu and J. Yang, *J. Phys. Chem. Lett.*, 2020, **11**, 4070–4079.
- 64 X. Zhu, F. Li, Y. Wang, M. Qiao and Y. Li, *J. Mater. Chem. C*, 2018, **6**, 4494–4500.
- 65 M. Kar, R. Sarkar, S. Pal and P. Sarkar, *Phys. Rev. B*, 2020, **101**, 195305.
- 66 A. Bafekry, M. Faraji, D. M. Hoat, M. Shahrokhi, M. M. Fadlallah, F. Shojaei, S. A. H. Fegghi, M. Ghergherehchi and D. Gogova, *J. Phys. D: Appl. Phys.*, 2021, **54**, 155303.